Draft version April 5, 2024
Preprint typeset using LaTeX style emulateapj v. 5/2/11

RESOLVING GAS FLOWS IN THE ULTRALUMINOUS STARBURST IRAS23365+3604 WITH KECK LGSAO/OSIRIS†

Crystal L. Martin[1] and Kurt T. Soto[2]

Draft version April 5, 2024

ABSTRACT

Keck OSIRIS/LGSAO observations of the ultraluminous galaxy IRAS 23365+3604 resolve a circumnuclear bar (or irregular disk) of semimajor axis 0.″42 (520 pc) in Paα emission. The line-of-sight velocity of the ionized gas increases from the northeast towards the southwest; this gradient is perpendicular to the photometric major axis of the infrared emission. Two pairs of bends in the zero-velocity line are detected. The inner bend provides evidence for gas inflow onto the circumnuclear disk/bar structure. We interpret the gas kinematics on kiloparsec scales in relation to the molecular gas disk and multiphase outflow discovered previously. In particular, the fast component of the ouflow (detected previously in line wings) is not detected, adding support to the conjecture that the fast wind originates well beyond the nucleus. These data directly show the dynamics of gas inflow and outflow in the central kiloparsec of a late-stage, gas-rich merger and demonstrate the potential of integral field spectroscopy to improve our understanding of the role of gas flows during the growth phase of bulges and supermassive black holes.

1. INTRODUCTION

Gravitational torques generated during galaxy mergers provide a widely accepted mechanism to transport gas from the outer regions of galaxies inwards where it can fuel the growth of stellar bulges and supermassive black holes (Springel et al. 2005; Hopkins et al. 2006; Hopkins et al. 2010). This growth is likely regulated by feedback from the starburst and active galactic nucleus, or AGN (Tremaine et al. 2002; Di Matteo et al. 2005, 2008). Accurately modeling these gas inflows and outflows remains central to understanding how gas dynamical processes shape the structural properties of galaxies. Resolving these flows during the peak era of bulge formation at $z \sim 2$ is not practical, so we study local analogs in order to better understand the dominant physical processes.

Galaxies with exceptionally high central concentrations of star formation, gas, and dust are rare in the local universe but have been identified by their high far-infrared luminosities, $L/\ \mathrm{L}_\odot \gtrsim 10^{12}$ (Soifer et al. 1986; Sanders et al. 1986; Solomon et al. 1997; Sanders et al. 1988b). This population of ultraluminous infrared galaxies (ULIRGs) selects major mergers of gas rich galaxies (Borne et al. 2000). The ULIRGs include a range of evolutionary stages from well-separated double nuclei to fully coalesced systems (Murphy et al. 1996; Veilleux et al. 2002). Towards later merger classes, the average contribution of nuclear activity to the bolometric luminosity increases (Veilleux et al. 2009), supporting the long-standing conjecture that an active nucleus emerges fairly late in the evolutionary progression (Sanders et al. 1988a).

Spatially resolved spectroscopy of ULIRGs provides strong evidence for inflowing gas on scales from roughly 1 kpc to several tens of kpc. For example, the increasing strength of Balmer absorption lines with galactocentric radius (Soto & Martin 2010) reveals stellar age gradients which are inverted relative to the typical inside-out growth of disks (Larson 1976; Naab & Ostriker 2006; Matteucci & Francois 1989; MacArthur et al. 2004; Boissier et al. 2008). The relatively young ages in the central few kpc's of ULIRGs and the paucity of young stars at large radii implies that star formation is truncated in the outer disk several hundred Myr before the gas supply is depleted in the central kpc. Also, in contrast to the normal decline of metallicity with radius in galaxies, ULIRGs have shallower or even inverted metallicity gradients (Rupke et al. 2008; Rich et al. 2012). Between first and second pericenter passage, inflow of lower metallicity gas from large radii dilutes the central metallicity. Inflows therefore clearly transport gas from the outer disk into the central kpc of the merger remnant.

In numerical simulations of major mergers, the high central gas densities trigger gravitational instabilities forming features like bars, rings, and spirals on sub-kiloparsec scales. An accurate description of these gas inflows on circumnuclear scales requires proper treatment of the physics on considerably larger spatial scales because the gas fueling is typically driven by kiloparsec-scale features, and the formation and evolution of these kiloparsec-scale features is governed by the dynamics of the galactic disks on scales of order 10 kpc (Chapon et al. 2013; Emsellem et al. 2015). The hydrodynamic interaction with gas outflows driven by supernovae and/or stellar radiation compounds this computational challenge but may significantly delay the decay of the two supermassive black holes (SMBHs) from separations of a few hundred parsecs to a few parsecs (Roškar et al. 2015). Fueling by gravitational instability naturally delays the peak activity from the SMBH until star for-

† The data presented herein were obtained at the W.M. Keck Observatory, which is operated as a scientific partnership among the California Institute of Technology, the University of California and the National Aeronautics and Space Administration. The Observatory was made possible by the generous financial support of the W.M. Keck Foundation. The data were obtained with the OH Supressing Infrared Spectrograph (OSIRIS) behind the Laser Guide Star Adaptive Optics System

[1] Physics Department, University of California, Santa Barbara, CA 93106-9530
[2] Institute for Astronomy, ETH Zurich, Zurich 8093, Switzerland

mation and feedback substantially reduce the gas fraction, a timescale of order 10^8 yr on kiloparsec scales (Hopkins et al. 2012). Testable predictions of these theoretical models include (1) the identification of shocks on sub-kpc scales (via morphological features like bars, rings, and spirals for example), (2) the properties of gas outflows from these regions, and (3) their temporal evolution during the merger progression.

Directly observing this inflow on sub-kpc scales has only recently become possible. Using the Keck I and II adaptive optics (AO) systems to obtain near diffraction-limited data cubes, Medling et al. (2014) found that nuclear disks were common in those (U)LIRGS classified as late stage mergers. Stellar nuclear disks are young and indicate recent inflow. The gaseous component of nuclear disks plays an important role in angular momentum transfer and is critical for the coalesence of binary black holes (Chapon et al. 2013; Cole et al. 2014; Roškar et al. 2015). Circumuclear disks have effective radii of a few hundred parsecs and masses between 10^8 and 10^{10} $M_\odot$ (Medling et al. 2014). The formation of this dynamically cold component of gas and stars in the nucleus appears to be required for triggering Seyfert activity (Hicks et al. 2013). Nuclear spirals, which are shocks in a circumnuclear disk, appear to be a common mechanism for feeding in the gas (Martini & Pogge 1999; Maciejewski 2004a).

Resolving scales of roughly 100 pc in both active galaxies (Müller-Sánchez et al. 2011; Davies et al. 2014) and ULIRGs (Cazzoli et al. 2014; Medling et al. 2015; Garcia-Burillo et al. 2015) has provided new insight about gas transport out of the central region. Müller-Sánchez et al. (2011) resolved emission from the narrow line region (NLR) and coronal line region of nearby AGN; the velocity fields of the NLR showed both disk rotation and bipolar outflows. In a study of a nearby buried quasar, F08572+3915:NW, Rupke & Veilleux (2013) found a close correspondence between the velocities of the blueshifted $H_2(1-0)$ emission component mapped with OSIRIS and the Herschel OH line profile of Veilleux et al. (2013), whereas optical emission and absorption lines traced a different part of the wind.

Galactic winds are ubiquitous among ULIRGS (Martin 2005; Rupke et al. 2005; Soto et al. 2012; Bellocchi et al. 2013; Veilleux et al. 2013; Rich et al. 2014; Cicone et al. 2014). The physical relationship between the outflowing gas mapped over scales of many kpc (Martin 2006; Rupke & Veilleux 2015) and the activity in the circumnuclear region of ULIRGs, however, remains relatively unexplored. Connecting high-resolution data cubes with the global gas kinematics may prove particularly interesting for those ULIRGs with very broad, blueshifted emission-line wings. Detections of similar features in spectra of high-redshift galaxies have recently been attributed to AGN (Genzel et al. 2014), whereas the strength and profile of the wings in Lyα spectra of cool ULIRGs is more simply understood in the physical context of gas condensing out of the hot phase of winds (Martin et al. 2015; Thompson et al. 2015). In the latter scenario, the highly blueshifted ($|v| > 500$ km s^{-1}) gas cools at radii of a few kpc, whereas AGN outflows are accelerated on much smaller spatial scales. The velocities of molecular outflows have been shown to increase with the luminosity of the active nucleus (Veilleux et al. 2013), but understanding whether the molecular gas is accelerated near the nucleus or forms in situ in the cooling wind at much larger radii requires spatial mapping.

In this paper, we seek to combine the resolution offered by adaptive optics with information from the wider fields obtained with seeing-limited observations and thereby identify signs of gas flows over several decades in radius. We present the gas kinematics and continuum morphology in the central region of IRAS 23365+3604, a ULIRG with a low central metallicity (Rupke et al. 2008) and inverted stellar age gradient (Soto & Martin 2010), at roughly 100 pc resolution. Archival images from the Hubble Space Telescope (HST, PROPOSID 10592 and 6346) facilitate identification of a suitable tip-tilt star for the AO system, enable accurate positioning of the OSIRIS (OH-Suppressing Infra-Red Imaging Spectrograph, Larkin et al. (2006)) lenslet array, and allow construction of a high-resolution color map. The redshift of the system shifts the Paschen-α 1875.13 nm emission into a relatively clean region of the airglow spectrum in the K band where we observed.

In §2 we describe the new Keck/OSIRIS observation. Measurements of the continuum morphology and the Paα morphology and kinematics are described in §3. We argue that the overall velocity field reveals an outflow launched from a circumnuclear disk, and that the disk shows signs of gas inflow. In § 4, we discuss the physical relationship of the associated gas flows to previous observations of this system on larger spatial scales. In § 5, we summarize our main results. Throughout this paper we adopt a ΛCDM cosmology with $H_0 = 70$ km s^{-1}Mpc^{-1}, $\Omega_m = 0.30$, and $\Omega_\Lambda = 0.70$. We adopt the CO redshift, $z = 0.064480$ (Solomon et al. 1997), which gives an angular scale of 1.239 h_{70}^{-1} kpc per arcsecond. Throughout the manuscript we define the position angle (PA) on the sky as the angle measured eastward from north.

2. DATA

The HST image and color map in Fig. 1 illustrates the environment of the region mapped in Paα. Tidal features are plainly visible to the south and southeast; a deep stretch of the contrast shows additional tidal features to the northeast. The stellar population has already aged several hundred Myr in much of the outer galaxy (Soto & Martin 2010). Along the ESI slit shown, Hα emission is detected from the tidal feature located roughly 6″ north of the nucleus and from the southern tidal arm. This tidal, ionized gas has a velocity gradient opposite in sign to the shear along the inner contours, and this counter rotation is shared by the molecular gas on comparably large spatial scales (see position-velocity diagram in Fig. 3 of Cicone et al. (2014)).

Table 1 summarizes the properties of IRAS 23365+2604. The high L_{FIR} indicates a star formation rate (SFR) over a hundred $M_\odot$ yr^{-1}. At this rate, the molecular gas supply will be exhausted on a timescale of 100 Myr, so we are clearly observing an object undergoing a rapid transition towards a more quiescent state.

2.1. *Observations*

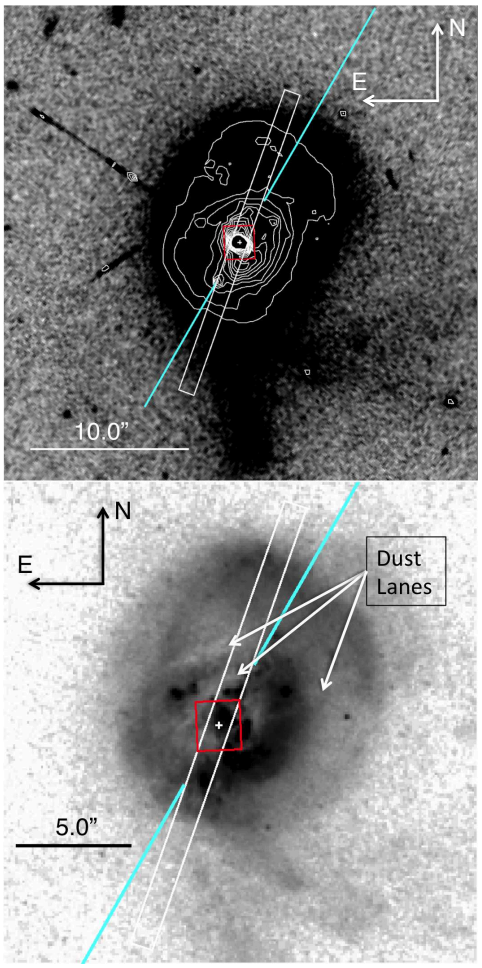

FIG. 1.— *Top:* HST F814W image of IRAS 23365+3604 with contours showing isophotes. The cyan line marks the major axis of the galaxy at $PA = -30°$. The red box indicates the $2\farcs10 \times 2\farcs24$ region mapped with OSIRIS. The white rectangle indicates the position of the slit used to obtain the echellete spectrum previously discussed by Martin (2005), Martin (2006), Soto & Martin (2010), Soto & Martin (2012), and Soto et al. (2012). *Bottom:* Map of $B - I$ color constructed from archival ACS/F435W and WFPC2/F814W HST observations. Two prominent dust lanes (white) are visible $1\farcs5$ and $3\farcs0$ northeast of the nucleus; a fainter dust lane approaches the southwest corner of the OSIRIS map (red box).

TABLE 1
IRAS 23365+3604

Property	Value
Redshift[a]	0.064480
$\log(L_{IR}/L_\odot)$[b]	12.20
$\log(L_{FIR}/L_\odot)$[c]	11.96
SFR ($M_\odot$ yr^{-1})[d]	280
$F_\nu(12\mu m)$ (Jy)	$\leq$ 0.25
$F_\nu(25\mu m)$ (Jy)	0.81
$F_\nu(60\mu m)$ (Jy)	7.69
$F_\nu(100\mu m)$ (Jy)	8.19
W(Na I) (Å)[e]	4.5 ± 0.4
V_{max} (Na I) (km s^{-1})[f]	-651
V_B (Na I) (km s^{-1})[g]	-389 ± 72
ΔV_B (Na I) (km s^{-1})[h]	-308 ± 85

[a] The redshift derived from a CO (1-0) observations (Solomon et al. 1997)
[b] Estimated 81000 μm luminosity. The IRAS 12 μm flux is an upper limits, so the median flux ratios of bright ULIRGs with IRAS detections in all four bands were used to estimate L_{IR} as described in Murphy et al. (1996).
[c] Far-infrared luminosity computed from $L_{FIR} = 3.86 \times 10^5 d_L^2[2.58F_\nu(50\mu m) + F_\nu(100\mu m)]L_\odot$, where the flux density is in Janskys and the luminosity distance is in Mpc.
[d] Star formation rate estimated from $SFR(\ M_\odot\ \mathrm{yr}^{-1}) = L_{IR}/5.8 \times 10^9\ L_\odot$ Kennicutt (1989). This relation assumes continuous star formation and a Salpeter initial mass function from 0.1 to 100 $M_\odot$.
[e] Equivalent width of interstellar resonance absorption in Na I $\lambda\lambda 5890, 96$ (Martin 2005).
[f] The maximum blueshift of the Na I absorption trough (Martin 2005).
[g] The blueshift of the fit to the interstellar, Na I absorption trough (Martin 2005).
[h] The width of the interstellar Na I absorption line (Martin 2005).

We observed IRAS 23365+3604 at Keck II on September 3, 2010 using the OSIRIS grating in third order with the Kn1 filter and the laser guide star adaptive optics (LGS-AO) system (Wizinowich et al. 2006) as described by Table 2. Conditions were clear; and the atmospheric seeing improved slowly over the course of the night from an initial value of approximately $0\farcs80$ FWHM. We configured OSIRIS with the $0\farcs035$ lenslet array which slightly undersamples the diffraction limited core of the point spread function (PSF) but enlarges the field of view of the 36×64 lenslet array to $1\farcs26 \times 2\farcs24$ per pointing. We obtained 2292 spectra at each pointing covering the complete spectral range from 1955 - 2055 nm at 0.25 nm per pixel.

We established the offset between the field of view of this Kn1 configuration and the center of the instrument field of view by observing a bright star with the Kn3 filter ($0\farcs020$ scale) and comparing this to the same object acquired in the Kn1 configuration (and matched $0\farcs020$ scale). Using this offset we acquired the tip tilt star in spectroscopic mode using the Kn1 filter ($0\farcs035$ scale), offset to the galaxy position defined by the nucleus in the F814W image, and tweaked the position to center the object in the Kn1 filter.

Using two pointings offset along the shorter dimension of the lenslet array, we mapped a $2\farcs10 \times 2\farcs28$ region (2.60 kpc $\times$ 2.83 kpc) centered on the brightest continuum knot. At each position, we dithered exposures in a box pattern with step size $0\farcs070$ along the axes of the lenslet array. The individual exposure times were 900 and 750 s, respectively, for the eight western and seven eastern positions. Since the entire field of view is covered by the object, leaving no empty sky spaxels, we employed an object/sky/object nodding pattern (of a few arc min-

TABLE 2
OBSERVATIONS

Name (1)	UT Date (2)	t_{exp} (3)	n_{exp} (4)	t_{tot} (5)	offset (6)	PA (7)	Filter (8)	Scale (9)
23365+3604:West	09-03-2010	900	8	7200	0.5	272	Kn1	0.035
23365+3604:East	09-03-2010	750	7	5250	-0.5	272	Kn1	0.035

NOTE. — Col.(1): IRAS name:pointing. Col.(2): Universal time observation date. Col.(3): Exposure time per dither/sky location in seconds. Col.(4): Number of target exposures. Col.(5): Total target exposure time in seconds Col.(6): Pointing offset from the nucleus of the galaxy. Each exposure was dithered in a box pattern by 0.″035 in the lenslet array x and y coordinate system around this central location. Col.(7): Position angle of the lenslet array in degrees. Col.(8): Spectrograph filter. Col.(9): Spatial scale of the lenslet array in units of arcseconds

utes).

The LGS-AO system produced an artificial guide star directly on the OSIRIS optical axis. We locked the tip-tilt sensor onto a natural guide star of magnitude $r = 16.7$ at an angular separation of 55.″2 from the nucleus and observed with a closed AO feedback loop. Between the last exposure at the western pointing and the first exposure at the eastern pointing, we observed a pair of stars with similar angular separation and PA as IRAS 23365+3604 and **its** tip-tilt star in order to characterize the PSF. We also performed repeated observations of two A0 stars at similar airmass as the target.

2.2. *Data Reduction*

Individual exposures were first reduced using Version 2.3 of the OSIRIS data reduction pipeline (Larkin et al. 2006). The presence of the bright galaxy, which covered a significant fraction of the detector, skewed the pipeline calculation of the offset level in each channel.[4] To circumvent this problem, we identified the subregions of each channel least affected by the galaxy and calculated the offset level using iterative sigma clipping. We treated these offsets as bias levels and subtracted them from each channel prior to re-processing with the pipeline. The pipeline processing included steps for sky subtraction, cosmic ray removal, spectral extraction, dispersion correction, telluric feature removal, and datacube construction. Observations of HIP114714 and HIP1603 were used to remove telluric features from the data cubes obtained at the western and eastern pointings, respectively.

We registered the individual datacubes produced by the pipeline using the telescope offsets commanded between the pointings and dither positions; these shifts were, by design, an integer number of spaxels for the PA of the lenslet array. To flag voxels (volume elements) with non-physical values in each cube, we calculated the median intensity and standard deviation among the individual cubes at each voxel. We constructed the final datacube from the aligned cubes using a single iteration of a 100σ mean clip to reject unphysical voxels (typically bad lenslets). We adopted the standard deviation among the individual datacubes, which was slightly larger than the error estimates produced by the pipeline, as the best estimate of the uncertainty in the intensity in each voxel.

2.2.1. *Dispersion Solution and Spectral Resolution*

To check the dispersion solution, we measured the centroids of five OH lines in the final datacube. The measured lines include the OH transitions near the observed $Pa\alpha$ emission at vacuum wavelengths of 2000.8163 nm and 2003.3211 nm (Rousselot et al. 2000). We found that the pipeline solution was too red and applied an offset of -0.527 nm to the dispersion solution.[5] We computed and applied a heliocentric correction of 13 km s^{-1}.

The spectral resolution has significant variation between lenslets and at different wavelengths. We measure a median linewidth of 100 km s^{-1} near the observed wavelength of Paα, consistent with the expected value of $R = 3100$ (cf., OSIRIS User Manual Figure 2-7).

2.2.2. *PSF Estimation*

Knowledge of the PSF is required to model how observed spatial structure relates to the intrinsic morphology. Since the wavefront reference for our observations is not the science target, constructing the PSF from the wavefront reference would be misleading due to anisoplanaticism. Instead, we observed a pair of stars, the "PSF pair", near our field (within 15°) from the 2MASS Point Source Catalog; this pair has a separation (within 5.″0) and PA (within 15°) very similar to that of IRAS 23365+3604 and its tip-tilt star (see Table 3). The "PSF tip-tilt star" plays the same role as the tip-tilt star used in the galaxy observation. It provides low-order corrections for the LGS system and must have a similar color and magnitude to that of the science tip-tilt star to ensure a similar distribution of flux on the wavefront sensor during the PSF-pair and science observations. Table 2 illustrates the close match in color and magnitude of the two tip-tilt stars.

We expect the AO system to deliver a PSF with a narrow core and broad wings (Davies et al. 2007). The diffraction limit of the telescope and detector pixel sampling shape the core. Natural seeing determines width of the halo. Figure 2 shows the PSF of the PSF star. A Moffat function fitted to the profile yields a core of width 0.″090 FWHM wide. The median profile plausibly shows wings over the scale of the natural seeing. We avoid any direct estimate of the Strehl ratio because it is sensitive to errors in background level; and variations in the sky intensity between our object and sky frames produce small errors in the background that are difficult to quantify.

In our analysis of IRAS 23365+3604, we model the AO PSF with a Gaussian function of FWHM matched

[4] The detector is read out in 32 channels. Each region has a slightly different zero-level intensity.

[5] This bug was fixed in a later version of the pipeline.

TABLE 3
PSF Stars

type (1)	name (2)	RA (3)	Dec (4)	b-r (5)	b-v (6)	r (7)	$\Delta\theta$ (8)	PA (9)
tip tilt	23385679+3621232	23 38 56.80	+36 21 23.26	0.5	0.28	16.7	55.9	210
PSF tip tilt	23301627+3648251	23 30 16.27	+36 48 25.11	0.4	0.22	16.4	56.45	210
PSF	23302096+3648229	23 30 20.97	+36 48 22.90	0.6	0.33	16.7		

Note. — Col.(1): The type of calibration that the star will be used for. Col.(2): 2mass PSC name Col.(3): Right Ascension Col.(4): Declination Col.(5): b-r color Col.(6): b-v color Col.(7): r band magnitude Col.(8): Angular separation between the target and the tip tilt star Col.(9): Position Angle of the tip tilt star relative to the target.

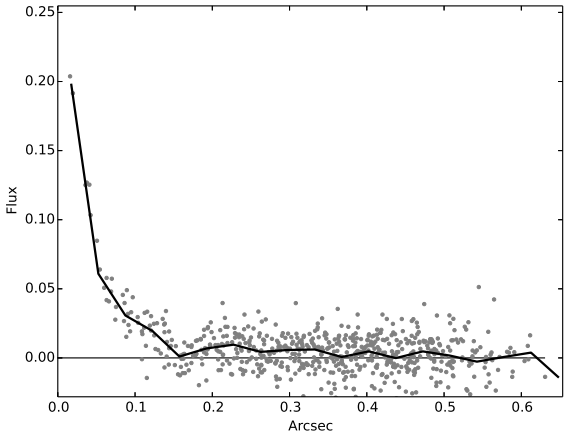

Fig. 2.— The radial profile of the PSF star. The gray points are the individual pixels of the PSF image. The black line is a median of azimuthal bins. The bin width, 0.″035, is matched to the lenslet scale. The core of the profile has a HWHM of 0.″045.

to the spatial profile of the PSF star. This PSF is convolved with each intrinsic model before comparing the model to the observed datacube. This approximation for the width of the core of the PSF suffices because it is inevitably the simplicity of our disk model that limits how well the convolved model matches the observed data cube.

3. RESULTS

The aim of this work is to relate the gas kinematics in the nuclear region of a ULIRG to the galaxy as a whole. To provide context for the OSIRIS data cube, we show an i-band image of the region surrounding the OSIRIS map in Figure 3. The i-band morphology is complicated due to both the recent merger and spatial variations in extinction. Across the region mapped with OSIRIS, the i-band surface brightness contours are elongated northeast - southwest at $PA = 50°$. This elongation of the distribution of stellar light contrasts sharply with the distribution of molecular gas. Cicone et al. (2014) and Solomon et al. (1997) derived position angles of -55°and -45°, respectively, for the major axis of the molecular gas emission. The Cicone et al. (2014) CO(1-0) map obtained with the IRAM PdB interferometer covers a field ten times larger than our OSIRIS map. We have sketched the beam size of Cicone et al. (2014)'s CO (1-0) observation in Panel (a) of Figure 3 to emphasize that the molecular gas measurements do not resolve the gas kinematics within the OSIRIS map.

3.1. *Description of the Morphology*

Panels (b) and (c) of Fig. 3 show the smoothed OSIRIS data cube. We experimented with several adaptive smoothing algorithms but show the result of smoothing over each 3×3 block of spaxels at each wavelength slice. The smoothing scale of 0.″105 maintains useful resolution in the circumnuclear region while improving the signal-to-noise ratio of the Paα nebula in the central kiloparsec. Using this smoothed data cube, we fit a first-order polynomial to the continuum level on either side of the line and a single Gaussian line profile. The fitted continuum level defines the line-free, K-band, continuum intensity, and the fitted flux defines the intensity of the $Pa\alpha$ image.

3.1.1. *Continuum Emission*

The continuum image shows a single nucleus. The FWHM of the point spread function in the OSIRIS image is 0.″091, so we estimate a maximum nuclear separation of $1.22 \times FWHM$, a physical length of 138 pc. As suggested by the single nucleus morphology in seeing-limited K-band and R-band images, this galaxy is at a late stage of merging, after the nuclei have coalesced (Murphy et al. 1996; Soto & Martin 2010; Zamojski et al. 2011). It is a Class IV Merger in the system described by Veilleux et al. (2002).[6]

The K-band continuum isophotes are shown by black contours in Panels (d) and (e) of Fig. 3. The major axis runs northwest – southeast at $PA = -46°$, which is remarkably well aligned with the galaxy major axis on large scales (indicated in Fig. 1). The K-band isophotes are clearly not showing the same features as the F814W contours which run nearly perpendicular to them. We attribute the very different morphologies of the optical and infrared images to the extremely high extinction in the ULIRG.

We fit the K-band image with Sersic profiles of fixed index n. Each parametric model was convolved with a Moffat profile of 0.″09 FWHM (to approximate the OSIRIS psf) before comparing to the data. The continuum surface brightness at radii $R \leq$ 0.″5 is well fitted by the exponential model ($n = 1$) with radial scalelength R_e = 0.″130 (161 pc). The surface brightness profile flattens at larger radii. The break in slope indicates a distinct morphological component that defines the circumnuclear region.

The size of this circumnuclear component is similar to that of nuclear disks. Medling et al. (2014), for ex-

[6] We note that Soto & Martin (2012) list this object as Class IIIb in their Table 1 based on spatial information in an optical spectrum, but the absence of two nuclei in the higher resolution imaging presented here is inconsistent with a Class III Pre-Merger stage.

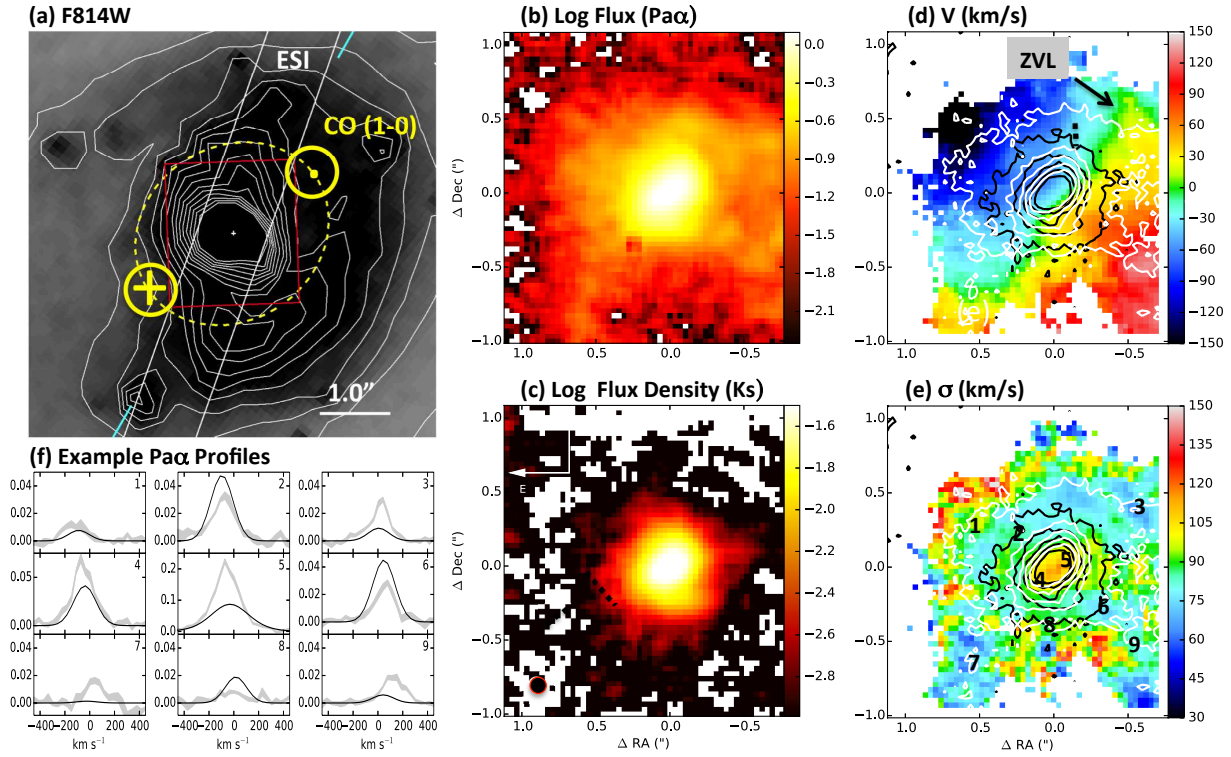

FIG. 3.— *(a)* HST F814W image from Fig. 1 zoomed in on the central 6.″0 by 6.″0 (7.4 kpc × 7.4 kpc) region of IRAS 23365+3604. Cyan ticks define the galactic major axis as in Fig. 1. The yellow ellipse indicates the beam size of the CO (1-0) observation of Cicone et al. (2014) who identify a disk of molecular gas with line of nodes at $PA = -55°$; the northwest side is approaching, and the southwest side receding. Red box indicates the size of the 2.″10 × 1.″90 field of the OSIRIS map. *(b,c)* The smoothed Paα line image and the line-free, K-band continuum, respectively The origin is the infrared nucleus; the circle in the lower left corner of Panel c indicates the resolution. The flux scales are logarithmic with arbitrary zero points, and the regions with fluxes smaller than the 1σ flux error are masked. *(d)* Doppler shift of Paα emission. The gradient in the line-of-sight velocity is along $PA = -34°$ and perpendicular to the contours of infrared continuum (black) and line (white) emission. The surface brightness contours have been drawn at 90%, 70%, 50%, 30%, and 10% of their peak values. The colorbar shows the zero velocity line in green, and we have masked spaxels with uncertainties greater than 10 km s^{-1}. See text for further discussion of the offset of the kinematic center from the position of the infrared nucleus. *(e)* Velocity dispersion, σ(km s^{-1}), of the Paα emission. For comparison, the instrumental linewidth of 100 km s^{-1} FWHM corresponds to $\sigma = 42$ km s^{-1} and is indicated by the dark blue shading. Numbers show the locations of the example line profiles. *(f)* Nine examples of Paα line profiles extracted from the data cube (gray) overlaid with the model (black) from Sec. 4.2. Comparison of the profiles at positions 4 and 5 across the central, non-axisymmetric structure show no velocity offset, consistent with their placement along the direction of the ZVL. Line profiles extracted near the prominent filaments, labeled 1, 3, 7, and 9, confirm both the overall sense of the velocity gradient across the OSIRIS map and the broader width of the observed lines (relative to the disk model).

ample, identified nuclear disks in nearby (U)LIRGs and measured effective radii of a few hundred parsecs. If the circumnuclear structure in IRAS 23365+3604 is intrinsically round, then the ratio of the semi-minor to semi-major axis implies a disk inclination of approximately 38°. Medling et al. (2014) measured rotation in both the stellar and gaseous components of the nuclear disks. We will examine the kinematics of the ionized gas in the circumnuclear structure in Sec. 3.2 below.

3.1.2. *Morphology of Ionized Gas Emission*

Like the K-band continuum isophotes, the highest surface brightness Paα isophotes are elongated in the southeast – northwest direction. The contours, shown by white isophotes in Fig. 3, have nearly the same position angle and centroid as the continuum emission. The Paα emission is detected at high S/N ratio to larger radii than the continuum emission. The Paα isophotes become nearly circular as the radius increases from 0.″224 ($R = 278$ pc) to roughly 0.″350 ($R \approx 434$ pc). This change in the ellipticity indicates the image of the ionized gas may be a superposition of multiple structures.

To characterize the size scale of these structures, we fit concentric ellipses to the image and produced a radial Paα surface brightness profile. We obtained a good fit with an exponential function on scales $R < 0.''42$ (520 pc); the scale length ($R_e = 0.''200$ or 248 pc) was slightly larger than measured for the stellar circumnuclear disk. The surface brightness profile flattens from $R = 0.''42$ (520 pc) to $R = 1.''00$ (1240 pc), and we fitted a scalelength $R_e = 0.''34$ (421 pc). The source of this flattening is the lower surface brightness Paα emission, clearly visible on scales $R > 0.''35$ in Fig. 3.

We will refer to this lower surface brightness emission as the *extended emission* in contrast to the higher surface brightness *circumnuclear emission* at $R < 0.''42$. The ex-

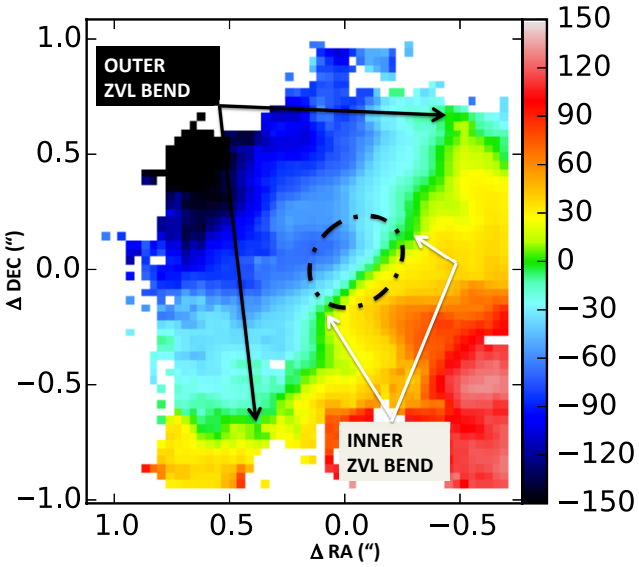

FIG. 4.— Two pairs of bends in the zero velocity line are highlighted by the green contour in the Paα velocity map. Gas on circular orbits in a disk would produce a straight ZVL. When the velocity field of the gas includes a radial inflow component, as in barred galaxies, kinks in the ZVL as seen here are often detected. In i23365+3604, the inner bend is located at the break in the infrared surface brightness which defines the circumnuclear region (dot-dashed ellipse with semi-major axis of 520 pc). The outer pair of kinks in the ZVL are located 0.″79 (0.97 kpc) from the nucleus where the ZVL makes a right angle turn clockwise, takes on a $PA \approx 44°$, and then reaches the outer edge of the OSIRIS map.

tended Paα emission at $PA \approx -90°$ is clearly visible in Fig. 3b over a kiloparsec to the western edge of the map. We will produce a sharper view of the filamentary structures when we subtract a smooth Paα emission component in Sec. 4.2.

3.2. *Description of the Paα Gas Kinematics*

We adopt the CO (1-0) redshift of $z = 0.064480$ from Solomon et al. (1997) to define the systemic velocity. Since this observation is integrated over the entire galaxy, we expect it to indicate the true barycenter of the ULIRG. We assign a systematic uncertainty of 17 km s^{-1} to this redshift, however, based on an unpublished redshift of $z = 0.064419$ kindly derived for us from another CO data cube (C. Cicone, pvt. comm.)

The central wavelength of our integrated Paα profile agrees with the near-infrared spectrum presented by Murphy et al. (2001). With the above definition of the systemic velocity, the integrated Paα line profile is blueshifted 30 km s^{-1}. The net blueshift would be reduced to 13 km s^{-1} had we adopted the $z = 0.064419$ redshift, so we claim a net blueshift of $13 - 30$ km s^{-1} for the ionized gas in the central kiloparsec relative to the molecular gas on galactic scales. The nucleus is not optically thin in Paα, and we interpret the blueshift of this Paα emission as evidence for a net outflow along our sightline. The redshift of the optical emission lines extracted from the nuclear aperture of the ESI spectrum is consistent with our Paα measurement.

We fit a Gaussian line profile to the Paα emission in each spaxel of the data cube. We then constructed maps of the Doppler shift and velocity width of the line emission. Fig. 3 shows the results. Note that the average velocity dispersion of the Paα emission is roughly 90 km s^{-1} across the map in Panel *e* of Figure 3. The typical linewidth is therefore roughly 200 km s^{-1} FWHM and significantly broader than the line spread function. The macroscopic velocity gradient is insufficient to broaden the lines this much, so the ionized gas must have a significant turbulent component.

3.2.1. *Circumnuclear Gas Kinematics*

In the circumnuclear region of Fig. 4, the zero velocity line (ZVL) of the Paα emission runs northwest – southeast at $PA = -46°$, but comparison to the continuum and Paα contours in Fig. 3d indicates the ZVL is offset southwest of the maximum infrared surface brightness. This offset persists if we adopt the Cicone et al. (2014) redshift; however, the ZVL moves towards the nucleus, closing about half the gap in Fig. 3d. A blueshift observed directly towards the nucleus, regardless of its exact size, is consistent with gas outflow on the near side of the circumnuclear disk. It is also possible that the circumuclear disk is simply offset relative to the barycenter of the merger.

Another surprising feature of the ionized gas kinematics in the circumnuclear region is the alignment between the velocity gradient and the *minor* axis of the infrared emission, which have the same position angle to within 10°. Nuclear disks, in contrast, typically show a velocity gradient along their major axis. The Paα velocity dispersion in the circumnuclear region of IRAS 23365+3604 is approximately 110 km s^{-1}, but the velocity along the major axis of the isophotes varies by less than 20 km s^{-1}. For comparison, Medling et al. (2014) measured significantly higher ratios of circular to random motion, $v/\sigma = 1 - 5$, in circumnuclear disks. If rotation dominates the circumnuclear velocity field in IRAS 23365+3604, then the underlying spheroid of ionized gas must be prolate rather than oblate like a disk.

In Fig. 4, we draw attention to two pairs of bends in the ZVL; these features are robust to the exact choice for the systemic velocity. We interpret the coincidence of the inner bends and the structure identified morphologically in Sec. 3.1 as evidence for gas inflow onto a circumnuclear disk or bar. The ZVL bends at the edge of a bar due to the distinctly non-circular motion of gas entering the ring (Athanassoula 1992; Maciejewski 2004a). A comparison of the velocity field in the circumnuclear gas to Figures 6 and 9 of Davies et al. (2014) is instructive. Those authors qualitatively fit the S20 bar model of Maciejewski (2004b) to the velocity field of warm molecular gas in two active galaxies. They find the ZVL nearly aligned with the minor axis of the isophotes. In contrast, in the circumnuclear region of IRAS 23365+3604, the ZVL is aligned with the major axis of the isophotes. The bar interpretation therefore requires that the long axis of the bar is considerably foreshortened by projection on the sky; we estimate a bar diameter of $\approx$ 520 pc/$cos(36°)$, or 640 pc.

3.2.2. *Kiloparsec-Scale Gas Kinematics*

Fig. 4 shows how the ZVL bends again roughly 0.″8 from the nucleus. The symmetric shape with respect to the nucleus is again similar to the flow patterns induced

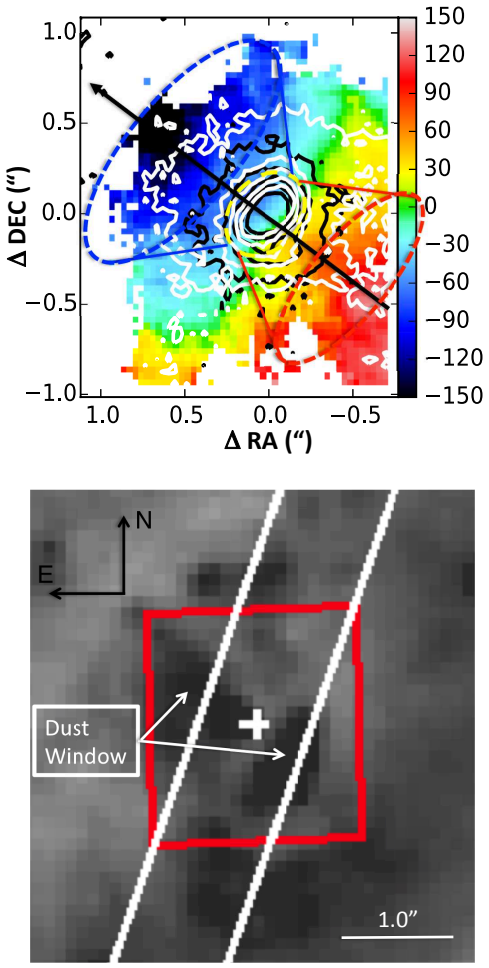

FIG. 5.— *Top:* The Paα velocity map with a schematic representation of an outflow from the circumnuclear disk. Contours are as defined in Fig. 3, and the black arrow indicates the velocity gradient through the nucleus. Feedback from young stars in the circumnuclear disk (yellow ellipse) drive the outflow into the approaching lobe (blue cone) and receding lobe (red cone). The PA of the Paα velocity gradient determines the axis of the bipolar flow. The outflow cone is drawn with an opening angle $\theta = 45°$ and include the ionized gas which blueshifted (redshifted) more the 50 km s^{-1} to the northeast (southwest). The largest blueshift is measured 0.″79 (0.97 kpc) northeast of the nucleus. With the northeastern lobe of the bicone tipped towards us, its superposition on the circumnuclear disk produces a net blueshift of the ionized gas towards the nucleus. *Bottom:* Color map from Fig. 1 zoomed for comparison to Paα gas kinematics. We detect blue $B-I$ color in two regions of the OSIRIS map. These two *dust windows* lie along the Paα velocity gradient. The outflow may have partially cleared out the dust here.

by bars. On this larger spatial scale, however, the infrared continuum is not deep enough in the OSIRIS cube to identify a non-axisymmetric, stellar structure. Near the location of the outer ZVL bend, however, the i-band isophotes in Fig. 3 twist from $PA \approx 50°$ (on smaller scales) towards the galactic major axis. The exact nature of this non-axisymmetric stellar structure is not clear, but we suggest that it causes the outer pair of bends in the ZVL. We believe these bends are the signature of gas inflow from the larger scale molecular disk down to sub-kiloparsec scales.

Our OSIRIS map lies within a single resolution element of Cicone et al. (2014)'s molecular gas map, so a direct comparison of the kinematics of the ionized and molecular gas is difficult. We simply note that from the velocity channels in the radio data, they find a disk of molecular gas at $PA = -55°$ with the northwest side approaching (as indicated in Fig. 3a). The line of nodes (LON), where the orbits intersect the plane of the sky, for this disk of molecular gas is nearly perpendicular (to within 10°) to the velocity gradient we see in the ionized gas at $PA = 44°$. Hence the Paα velocity gradient is not in the direction expected from the rotation of the molecular gas disk.

3.2.3. *Interpretation: Superposition of Outflow and Inflow*

The OSIRIS observation has resolved a kpc-scale structure of gas not previously identified in IRAS 23365+3604. Considering the chaotic situation in the central kiloparsec of a merger, the regular nature of this velocity gradient merits an explanation. Keeping in mind the considerably larger spatial scales of the molecular gas map, the kiloparsec-scale gas motion might reflect rotation in a barred disk; the disk and bar scales being set by the CO (1-0) and F814W inner isophotes, respectively. This interpretation would directly attribute the outer kinks in the ZVL to bar-induced gas inflow, suggesting a doubly barred system (Maciejewski et al. 2002; Maciejewski 2004b). We have several concerns, however, with this interpretation. First, the F814W isophotes do not have the regularity of bars in normal spirals; and, second, this scenario places a circumnuclear disk/bar within an outer bar that has an unusually small semimajor axis of just one kiloparsec. In addition, the molecular gas is the dominant mass component in the central kiloparsec, and it would have to be highly concentrated to explain the velocity gradient with orbital motion.[7]

A galactic outflow offers an alternative explanation for the Paα velocity gradient. The position angle of this velocity gradient suggests blowout perpendicular to the circumnuclear disk, i.e., along the path of least resistance. We sketch a schematic picture in Fig. 5. Projection of the northeastern lobe of the outflow against the circumnuclear disk also offers a plausible explanation for the blueshift of the ionized gas measured towards the infrared nucleus and the increase in velocity dispersion northeast of the nucleus. Another advantage of the outflow interpretation is that it does not require the ionized gas to be in virial equilibrium.

We find additional evidence for a bipolar structure, in contrast to an axisymmetric disk, in the dust distribution within the central kiloparsec of i23365+3604. Two regions of reduced reddening are identified on opposite sides of the nucleus in the lower panel of Fig. 5. These regions of bluer $B-I$ color are roughly a kiloparsec across.

[7] Cicone et al. (2014) estimate a molecular gas mass of $\log(M_{H_2}/\,\mathrm{M}_\odot) = 9.93$. Nearly all (90%) of the CO(1-0) emission comes from the central 5.″0 (6.20 kpc) diameter region. Based on the nuclear K' magnitude from Surace et al. (2000), the total stellar mass is of order 9.8×10^8 M$_\odot$ in this region; an estimate which seems reasonable in comparison to mass measurements of other circumnuclear disks, i.e., 10^8 to 10^{10} M$_\odot$ (Medling et al. 2014). From the gravity of the molecular gas alone then, gas on circular orbits would reach a rotation speed of 110 km s^{-1} at a radius of 3.1 kpc. Our map of the ionized gas velocity field shows higher Doppler shifts, however, within a kiloparsec of the nucleus.

Their offsets northeast and southwest of the nucleus are directly along the Paα velocity gradient. A similar reduction in reddening is seen in the circumnuclear regions of NGC 3227 and NGC 5643 where it has been attributed to an ionization cone produced by an outflow (Davies et al. 2014). The color map suggests the outflow cone has effectively displaced dust roughly one kiloparsec.

The outflow interpretation does not explain all the features in the data cube. It does not, for example, explain the bends in the ZVL, which we still attribute to inflow on both the kiloparsec and circumnuclear scales. Furthermore, while the wispy Paα filaments, visible in Fig. 3b and discussed further in Sec. 4.2, may turn out to be outflow features, we acknowledge that they do not line up closely with the cones sketched in Fig. 5. If the filaments are associated with an outflow, then the geometry is more complicated than the simple cone depicted in Fig. 5. We note some resemblances to Fig. 7 of Roškar et al. (2015) which shows a circumnuclear outflow in a simulation of a merger remnant; the gas flow is initially bipolar but takes on a more complicated appearance before traveling even a full kiloparsec due to the chaotic nature of the surrounding interstellar medium. We suggest that the Paα velocity field is the superposition of such an outflow and gas inflow towards the circumnuclear disk. Observations of AGN on similar spatial scales to our observation have shown combinations of molecular inflow and outflow superimposed on a rotating disk (Müller-Sánchez et al. (2011), Hicks et al. (2013), Rupke & Veilleux (2013), Davies et al. (2014), Medling et al. (2015)).

4. DISCUSSION

Previous observations of IRAS 23365+3604 have shown that the merger has induced gas inflow from large radii towards the central kiloparsec (Soto & Martin 2010) and that the starburst drives a galactic outflow which covers the entire galaxy (Martin 2006; Soto & Martin 2012). Analysis of the OSIRIS data cube reveals a circumnuclear disk or bar, the kinematic signature of gas inflow towards this structure, and evidence for a bipolar outflow emanating from it. We further discuss these resolved gas flows and their relationship to galactic gas kinematics in this section.

4.1. *Relationship of Nuclear Outflow to Galactic Wind*

The solid angle of the entire OSIRIS field of view is not much larger than a typical, seeing-limited spectroscopic aperture. The echellete spectrum (obtained along the slit position shown in Fig. 1) shows two signatures of galactic outflow: (1) a broad, blueshifted wing on the emission-line profiles and (2) blueshifted resonance absorption. We plot these line shapes relative to the systemic velocity in Fig. 6. The spectra shown were extracted from a seeing-limited observation of the nucleus; these outflow signatures have been mapped over several spatial resolution elements.

4.1.1. *Absence of Fast Outflow Detection in the Nucleus*

To match apertures, we overplot the integrated Paα line profile in Fig. 6. The core of the Paα and optical emission lines have the same Doppler shift and profile shape. The blueshifted wing on the optical lines extends to much larger Doppler shifts, reaching ≈ -700 km s^{-1}, than does the Paα line profile. The bulk Doppler shifts (± 150 km s^{-1}) detected in the OSIRIS map are not nearly as large as those of the blue wing on the optical line profiles. We do not detect the fast outflow marked by broad, blueshifted component in optical spectra in the OSIRIS data cube. The broad line components in the optical spectrum are almost exclusively shock excited (Soto et al. 2012). In contrast, the narrow component, which appears to be directly associated with the Paα profile, has line ratios indicative of photoionization by massive stars.

When we see deeper into the ULIRG in the near-infrared, this line wing turns out to be much less prominent than in the optical. This result is difficult to understand unless the narrow component is indeed more reddened than the highly blueshifted gas; in other words, the line wing becomes weaker relative to the core when we can probe deeper into the ULIRG. Based on its absence in the Paα map, the highly blueshifted gas is not coming from the unresolved nucleus.

Martin et al. (2015) proposed that the fast outflow was recently part of the hot wind fluid. The higher density in ULIRG winds, or any starburst with a high SFR surface density, allows the wind to cool down to the inflection in the cooling function around $10^{7.2}$ K where thermal instability leads to condensations within the hot wind. In this physical picture, the molecular component of the outflow (Veilleux et al. 2013; Cicone et al. 2014) may also form in situ in the fast outflows.

The Herschel-PACS observation of IRAS 23365+3604 shows a strong P-Cygni profile in the OH 119 μm $+^{18}$OH 120 μm complex. The blueshifted absorption troughs reach Doppler shifts up to -1300 km s^{-1}(Veilleux et al. 2013). The OH line profile integrates the signal from a $9'' \times 9''$ spatial region, however, so we re-examine the CO (1-0) map of Cicone et al. (2014) for clues about the physical location of the high velocity outflow. The 10% of the line flux not modeled by the Gaussian fit lies in low intensity line wings; detections in the channel maps over $-600 < V_{CO}($ km s$^{-1}) < -300$ show the highest velocity CO emission comes from a region east of the nucleus just beyond the region mapped with OSIRIS.

Resonance absorption from Na I must trace gas sheltered from the ionizing continuum, so we might expect some rough spatial association with the molecular outflow. Since the optical transition is a doublet, we show the fitted profile of only the λ5896 transition in Fig. 6 to avoid confusion from the blend. The systemic absorption covers a velocity range slightly broader than the narrow emission component. The velocity range of the outflow component matches that of the blue wing seen on the optical emission lines.

Martin (2006) mapped the Na I absorption across the ULIRG demonstrating that the outflow covers the galaxy and is not confined to the nuclear region. In their Fig. 1p, a spectrum of the nucleus (Aperture 3) shows a blueshifted component substantially stronger than the absorption at the redshift of the galaxy. Moving along the slit to the north, the systemic component grows in strength relative to the outflow component, whereas the outflow component continues to dominate the absorption trough towards the south (e.g., aperture 2). This velocity

shift of the trough along the slit is smaller, and in the opposite direction to, the gradient in the Hα Doppler shift as can be seen Fig. 2o of Martin (2006). The prominence of the Na I outflow to the south-southeast (along the ESI slit) is consistent with the low-ionization-state outflow being coincident with the CO outflow, which is mapped in Fig. 3c of Cicone et al. (2014).

4.1.2. *Properties of The Nuclear Outflow*

We can relate the gas kinematics in the Paα map to the structure seen in an Hα spectrogram, which is shown in Figure 1p of Martin (2006). Within $\pm 3''$ of the nucleus along the slit, the Hα is blueshifted (redshifted) to the northwest (southeast). Although Martin (2006) attributed this velocity shear as a combination of orbital and rotational motion in merging gas disks, the higher resolution view afforded by OSIRIS does not resolve two nuclei thereby ruling out this interpretation. The Paα map reveals the position angle of the velocity gradient is nearly perpendicular to that of the molecular disk. The shear in the Hα spectrum is consistent with the Paα map at the same PA.

The velocity gradient seen in our Paα map contributes to the width of the Paα line in the circumnuclear spectrum. The blueshifts (and redshifts) detected in the northeast (southwest) corner of the OSIRIS data cube are slightly larger than the velocity dispersion towards the brighter circumnuclear disk/bar. The effect is not large because the most Doppler shifted emission regions have relativley low surface brightness. The bulk motion, however, would clearly contribute to the linewidth in seeing-limited, spectroscopy of the circumnuclear region.

We expect to see gas outflow from the nucleus considering its well established presence on large spatial scales, so we briefly examine the consequences of such an interpretation. To the northeast, the Paα is blueshifted up to -150 km s^{-1}, and the Doppler shift reaches +150 km s^{-1} towards the southwest corner of the OSIRIS map. A model with a constant velocity outflow, in contrast, produces radial isovelocity contours. A successful outflow model must account for this velocity gradient along the axis of the outflow cone. Acceleration over spatial scales from about 100 pc up to a kiloparsec could be produced by the radiation pressure from a central concentration of stars as described by Murray et al. (2011); alternatively, velocity segregation in the flow would lead to higher velocity gas at larger radii (because it moves more quickly than low velocity gas).

In principle, for a particular parameterization of the radial velocity, one could fit the inclination and opening angle of the cone. Here, we estimate the outflow cone is tipped roughly 47° relative to our sightline based simply on the axis ratio of the stellar nuclear disk. If we assume an intrinsically round disk for illustration, then the inclination $i = 43°$, and we infer a radial outflow speed of 200 km s^{-1} for the ionized gas.

4.2. *The Formation of a Circumnuclear Disk:*

Our infrared observations resolve a non-axisymmetric, circumnuclear structure. Its size lies within the range of the nuclear disks identified recently by Medling et al. (2014) in LIRGs and ULIRGs. The structure of such disks is shaped largely by radiation pressure (Scoville

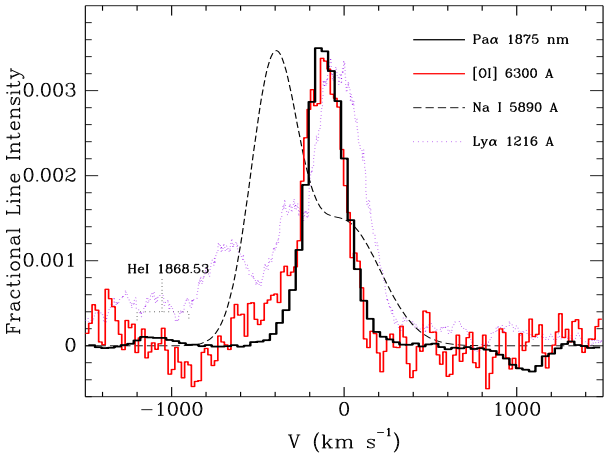

FIG. 6.— The integrated Paα line profile from the entire OSIRIS map compared to the optical [OI] emission line profile. The HeI1868.53 nm emission line is also detected in the line wing. The dashed line shows one component of the fit to the Na I doublet in a spectrum extracted from the nucleus; this is Aperture 3 as described in Martin (2006). The continuum level has been fit and subtracted in each case, and the resulting line profile normalized by the central intensity as measured by a fitted Gaussian profile. The [OI] profile is well fitted by two Gaussian components: (1) a narrow Gaussian ($\sigma = 81$ km s^{-1}) with a small Doppler velocity of $V = -39$ km s^{-1}, and (2) a blueshifted wing ($V = -290$ km s^{-1}) which is much broader, $\sigma = 290$ km s^{-1}(Soto et al. 2012). The broad, blue wing on the [OI] emission profile is not detected in the OSIRIS data cube. The broad wing is most prominent in the Lyα spectrum obtained through a $2''.5$ diameter aperture (Martin et al. 2015). The fitted Na I λ5890 profile is shown inverted to facilitate comparison of the absorption to the emission lines kinematics. The Na I shows a strong, blueshifted component at velocities similar to the blue wing on the optical emission-line profiles in addition to a component at the systemic velocity.

2003), and models including this process predict two classes of nuclear disks: (1) those with a starburst on large scales that consumes all of the gas with little or no fueling of a central AGN and (2) those with an outer large scale starburst accompanied by a more compact starburst on 1-10 pc scales and a bright central AGN Thompson et al. (2005). The circumnuclear disk in IRAS 23365+3604 appears to still be in the former state, and the cool infrared color of this ULIRG is consistent with the spatially extended starburst powering the majority of the bolometric luminosity.

We find signs of gas inflow onto this structure. The bends in the ZVL near this structure reveal deviations from circular motion, and similar features are expectated from the radial infall produced by nuclear bars and spirals. However, whereas Medling et al. (2014) observe rotation about the minor axis of the nuclear disks, the ZVL of our Paα map follows the major axis of the circumnuclear structure. In order to produce this offset between the LON and the major axis, a model of the circumnuclear structure in ı23365+3604 would appear to require an intrinsically non-axisymmetric component.

To better understand the nature of this circumnuclear structure, we considered the gas kinematical signatures of nuclear bars and spirals. For example, as gas responds to a non-axisymmetric potential, a nuclear spiral forms that may either be damped leading to the formation of a nuclear ring or get strengthened and propagate to-

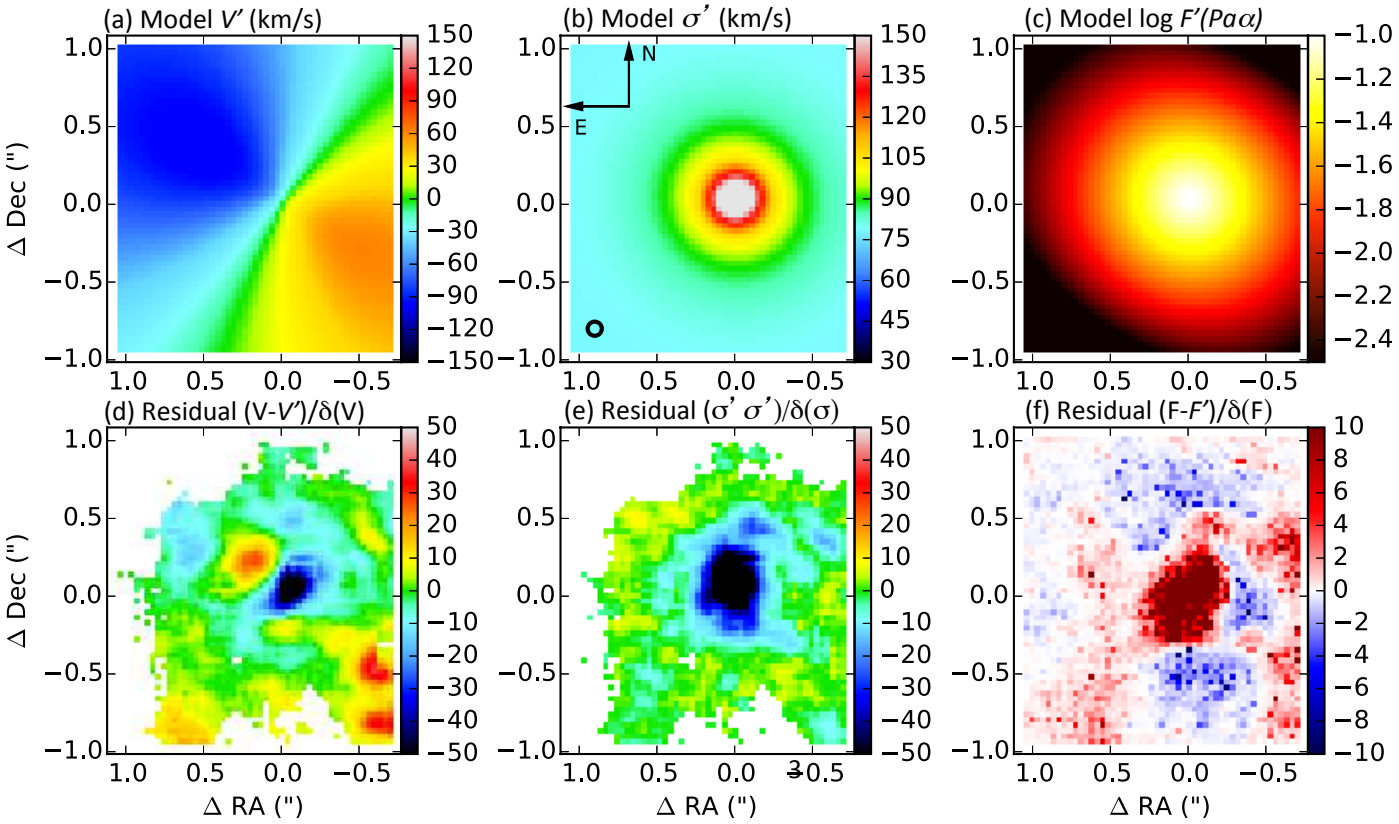

FIG. 7.— The velocity field, velocity dispersion, and surface brightness for a fitted disk (a-c) and the fit residuals as a fraction of the error (e-f). The spatial resolution of the data is indicated by the small circle in the lower, left corner of (b). The disk model adopts an exponential function to describe the radial decline in surface brightness. The surface brightness profile perpendicular to the plane of the disk scales as $\Sigma(z) \propto \exp(-0.5z^2/h_z^2)$, where the vertical thickness of this disk was fixed at a constant fraction of the half-light radius such that $h_z = 0.2R_{1/2}$. The line-of-sight velocity dispersion includes several terms, described in Table 4, to simulate the observed total velocity dispersion $\sigma_{\rm tot}$. Line profile comparisons are shown in Fig. 3.

wards the SMBH as a spiral shock Maciejewski (2004b). In the models shown in Figures 6 and 9 of Davies et al. (2014), the LON within the ring is along the major axis, and the ZVL is along the minor axis within the ring (opposite to what we see in IRAS 23365+3604). The ZVL bends abruptly at the ring due to the mostly radial inflow along the spiral arms at larger radii. To fit a similar model to our data cube, where the major axis is not along the LON, projection on the sky must significantly foreshorten the major axis. Hence, the circumnuclear structure would be intrinsically even less round than it appears in projection.

To look more carefully for signatures of spiral shocks feeding the circumnuclear disk, we fit a simple, disk model to the data cube. We used the GalPak ^{3D} code recently introduced by Bouché et al. (2015) and fit the intensity of the Paα emission in each voxel. GalPak^{3D} convolves an intrinsic model with a 3D kernel and returns a model data cube. We adjusted this kernel to describe the line spread function (LSF) and PSF of the OSIRIS observation. The LSF convolved with the combined spectra in the modeled disk produces emission lines at the instrumental spectral resolution of $\Delta V \approx 100$ km s^{-1}. The code uses a Markov Chain to efficiently explore parameter space. Uncertainties in the fitted parameters are estimated from the posterior probability distribution after 20,000 Monte Carlo iterations. We list the fitted parameters and their values in Table 4.

We subtracted this model from the data to highlight the non-axisymmetric structures as illustrated in Fig. 7. The circumnuclear disk dominates the residuals. The flux residuals in Panel *f* also reveal three filaments running approximately 1 kpc to the edge of the OSIRIS map and a fourth, shorter filament to the northeast. These filaments do not resemble spiral arms. The southwest and southeast filaments, if they were arms, would have very different pitch angles than would the western filament. Neither do we recognize a nuclear spiral in the color map shown in Fig. 5, whereas the nuclear spirals often found in the central kpc of active galaxies imprint a recognizable signature in color maps (Martini & Pogge 1999; Davies et al. 2014).

Velocity residuals offer another method for identifying nuclear spirals through a pattern of radial inflow and outflow in the plane of the disk (Davies et al. 2009). The velocity residuals in Panel *d*, however, show no correlations with the locations of the Paα filaments. The largest residuals correspond to the bluest regions in the $B-I$ color map in Fig. 5, and we attribute this correspondence to an outflow.

Finally, we would also expect local increases in velocity dispersion from the shocks associated with a bar or spiral shock. Because the infall maintains some angular momentum, it hits dense gas in the arm on the opposite side (Davies et al. 2009). The velocity dispersion residuals in Panel *e*, however, are largely axisymmetric. Figure 3f shows that the line profiles from the disk model are too broad in the nucleus and too narrow at large radii.

We conclude that the circumnuclear structure in ı23365+3604 although the size of a typical disk shows unusual gas kinematics which suggests it is not yet an axisymmetric disk. This ULIRG may be observed soon enough after the coalescence of the two cores that the circumnuclear disk has not completely reformed. Figure 9 of Roškar et al. (2015), for example, shows that a merger remnant can require up to 10 Myr to rebuild a regular disk. Those simulations predict that such structures contain two SMBHs separated by several tens of parsecs. Considering the inflow timescales measured for this galaxy on scales of several kiloparsecs (Soto & Martin 2010), we are observing ı23365+3604 roughly 100 Myr after the final passage.

5. SUMMARY

The spatial resolution delivered by the Keck AO system resolves a young, circumnuclear disk in IRAS 23365+3604. Its radial scalelength is $R_e = 0\farcs130$ (161 pc) in the starlight and ionized gas, and its position angle on the sky happens to nearly coincide with that of a molecular disk identified previously on much larger spatial scales (and at much lower spatial resolution) (Cicone et al. 2014). The isophotes of the ionized gas are rounder than the starlight and extend into filaments traceable over a kiloparsec to the edges of the Paα map .

The Paα line is blueshifted northeast of this circumnuclear disk and redshifted to the southwest. The large-scale velocity gradient of roughly 150 km s^{-1} per kiloparsec establishes the source of the shear previously observed in the Hα spectrum near the nucleus Martin (2006) and broadens the core of the photoionized line component in the circumnuclear spectrum. Remarkably, however, this gradient is nearly perpendicular to the major axis of both the infrared continuum and CO (1-0) isophotes, so it cannot mark the rotation of a oblate disk of ionized gas.

The isovelocity contours in the OSIRIS Paα map show significant deviations from regular motion. In particular, two sets of symmetric bends in the ZVL provide evidence for gas inflow into the circumnuclear region. The outer bends plausibly mark inflow into a gas bar previously unresolved in the CO (1-0) observation. Within this kiloparsec scale disk/bar, we found both kinematic and morphological evidence for a nuclear bar or irrgular disk.

The absence of a highly blueshifted wing on the integrated Paα line profile, or anywhere within the field mapped with OSIRIS, poses an interesting paradox. A prominent wing is visible on both the H Balmer lines and the optical forbidden lines in an ESI spectrum of the nucleus; and this high velocity outflow is shock excited (Soto & Martin 2012). Qualitatively, the high velocity outflow becomes more prominent relative to the line core at shorter wavelengths. It is most prominent in Lyα emission for example, where the core is likely depressed due to resonance scattering but the line wings appear to be direct emission (Martin et al. 2015). One possible explanation is that because we see a much larger volume of the nucleus in the near-infrared (due to the reduced extinction), the increased strength of the narrow line core leaves the emission in the line wing (potentially emitted by gas at much larger radii) much less prominent.

The starburst fueled by the galaxy merger over the past 100 Myr drives a previously studied global outflow. The Paα velocity gradient in the OSIRIS map provides evidence for a circumnuclear outflow emanating from a region where the circumnuclear disk is forming following the final coalescence of the galactic cores. Factors favoring this interpretation of the Paα emission include (1) the orientation of the Paα velocity gradient, which is consistent with a circumnuclear outflow collimated by the disk of molecular gas, (2) the net blueshift of the ionized gas emission towards the nucleus, and (3) the spatial correlation between the the steepest velocity gradient and the minimum reddening. For an outflow that dominates the Paα emission, we infer a launch region the size of the circumnuclear disk (radius 520 pc) and estimate an acceleration of roughly 150 km s^{-1} over one kiloparsec. Calculations for outflows from massive star clusters indicate the radiation pressure from just a few million $M_\odot$ cluster could easily produce this acceleration, see Figure 4 of Murray et al. (2011).

Alternatively, the Paα velocity gradient is due to gas orbiting in a bar-like structure roughly two kiloparsecs across. The position angle of the inner F814W isophotes offer a plausible, but not compelling, stellar component. The existing CO (1-0) observations lack the resolution to resolve even this kiloparsec-scale, non-axisymmetric structure. In the future, we hope to resolve the kinematics of the warm, molecular gas in $H_2(1-0)$ emission and elucidate the nature of the overall velocity gradient by resolving the morphology of the shocked gas in this dynamic environment.

Our results demonstrate that gas dissipation is a very important process for forming nuclear structures. We show that the patches of lower reddening in the circumnuclear region are spatially coincident with the circumnuclear outflow. We have caught the outflow sweeping dust away from the nuclear region where the nascent AGN remains highly obscured in this system. The irregular structure of the circumnuclear disk may reflect its youth, and we suggest ı23365+3604 would be an excellent target in which to look for a pair of SMBHs separated by a few tens of parsecs.

This research was partially supported by the National Science Foundation under AST-1109288. We thank Nicolas Bouché, Claudia Cicone, Eric Emsellem, and

TABLE 4
Fitted Parameters of Disk Models

(1) Disk Model	(2) R_d ($''$)	(3) i ($^\circ$)	(4) PA ($^\circ$)	(5) V_{max} (km s^{-1})	(6) σ_i (km s^{-1})	(7) χ_ν
Unmasked Mass	0.217 ± 0.001	22.1 ± 0.1	55.5 ± 0.1	197.8 ± 0.5	73.1 ± 0.1	4.64
Masked Mass	0.270 ± 0.001	20.0 ± 0.1	55.4 ± 0.1	243.1 ± 0.8	71.5 ± 0.2	3.88

Note. — Col.(1): We experimented with masking out the central region of the data cube and fitting only the large-scale velocity gradient. The masking improves the fit statistic but produces little change in best-fit disk parameters. Col.(2): Exponential radial scalelength. The radial scalelengths become systematically larger when the central Paα emission is masked, entirely consistent with the flattening of the Paα surface brightness profile described in Sec. 3.1.2. Col.(3): Disk inclination varies only slightly among models. Col.(4): Disk position angle (measured going east from north) varies only slightly among models. Col.(5): Asymptotic rotation speed computed using the *mass model* defined by $V(R) = \sqrt{\mathrm{G\ M}_{enc}(R)/R}$, where $\mathrm{M_{enc}(R)}$ is the mass within radius, R. This definition ties the velocity profile to the chosen surface brightness profile. In the model, $\mathrm{M_{enc}(R)}$ is determined numerically by summing the flux as a function of radius and assuming that the ratio of enclosed mass to Paα flux is constant with radius. This profile is then normalized to its maximum within the region modeled. Col.(6): The intrinsic velocity dispersion, σ_i, of the gas which accounts for the internal gas dynamics of the disk. The total velocity dispersion is defined as $\sigma_{\mathrm{tot}} = \sqrt{\sigma_d^2 + \sigma_i^2 + \sigma_m^2}$, which includes terms for mixing, σ_m, along the line of sight (appropriate to a geometrically thick disk) and the velocity dispersion produced by the disk self-gravity, $\sigma_d/h_z \equiv V(r)/r$. Col.(7): Reduced chi-squared fit statistic.

Roberto Maiolino for stimulating discussions that improved this manuscript. Alexander Adams contributed preliminary modeling which appeared in Soto (2012) and influenced the direction of our analysis. A portion of this manuscript was written while CLM visited the Aspen Center for Physics which is supported by the National Science Foundation under Grant No. NSF PHYS-1066293. We also acknowledge the very significant cultural role and reverence that the summit of Mauna Kea has always had within the the indigenous Hawaiian community. We are most fortunate to have the opportunity to conduct observations from this mountain.
Facilities: Keck

REFERENCES

Athanassoula, E. 1992, MNRAS, 259, 328
Bellocchi, E., Arribas, S., Colina, L., & Miralles-Caballero, D. 2013, A&A, 557, A59, 1307.1659
Boissier, S. et al. 2008, ApJ, 681, 244
Borne, K. D., Bushouse, H., Lucas, R. A., & Colina, L. 2000, ApJ, 529, L77
Bouché, N., Carfantan, H., Schroetter, I., Michel-Dansac, L., & Contini, T. 2015, ArXiv e-prints, 1501.06586
Cazzoli, S. et al. 2014, A&A, 569, A14, 1406.5154
Chapon, D., Mayer, L., & Teyssier, R. 2013, MNRAS, 429, 3114, 1110.6086
Cicone, C. et al. 2014, A&A, 562, A21, 1311.2595
Cole, D. R., Debattista, V. P., Erwin, P., Earp, S. W. F., & Roškar, R. 2014, MNRAS, 445, 3352, 1410.4339
Davies, R. I. et al. 2014, ApJ, 792, 101, 1407.2519
——. 2009, ApJ, 702, 114, 0903.0313
Davies, R. I. et al. 2007, ApJ, 671, 1388
Di Matteo, T., Colberg, J., Springel, V., Hernquist, L., & Sijacki, D. 2008, ApJ, 676, 33
Di Matteo, T., Springel, V., & Hernquist, L. 2005, Nature, 433, 604, astro-ph/0502199
Emsellem, E. et al. 2015, MNRAS, 446, 2468, 1410.6479
Garcia-Burillo, S. et al. 2015, ArXiv e-prints, 1505.04705
Genzel, R. et al. 2014, ApJ, 796, 7, 1406.0183
Hicks, E. K. S. et al. 2013, ApJ, 768, 107, 1303.4399
Hopkins, P. F. et al. 2010, ApJ, 724, 915, 1004.2708
Hopkins, P. F. et al. 2006, ApJS, 163, 1
Hopkins, P. F., Quataert, E., & Murray, N. 2012, MNRAS, 421, 3488
Kennicutt, R. C. 1989, Astrophysical Journal, 344, 685
Larkin, J. et al. 2006, NAR, 50, 362
Larson, . 1976, MNRAS, 176, 31
MacArthur, L. A., Courteau, S., Bell, E., & Holtzman, J. A. 2004, ApJS, 152, 175
Maciejewski, W. 2004a, MNRAS, 354, 883, astro-ph/0408098
——. 2004b, MNRAS, 354, 892, astro-ph/0408100
Maciejewski, W., Teuben, P. J., Sparke, L. S., & Stone, J. M. 2002, MNRAS, 329, 502, astro-ph/0109431
Martin, C. L. 2005, ApJ, 621, 227
——. 2006, ApJ, 647, 222
Martin, C. L. et al. 2015, ApJ, 803, 6, 1501.05946
Martini, P., & Pogge, R. W. 1999, AJ, 118, 2646, astro-ph/9909032
Matteucci, ., & Francois, . 1989, MNRAS(ISSN 0035-8711), 239, 885
Medling, A. M. et al. 2014, ApJ, 784, 70, 1401.7338
——. 2015, MNRAS, 448, 2301, 1501.07289
Müller-Sánchez, F. et al. 2011, ApJ, 739, 69, 1107.3140
Murphy, T. W. et al. 1996, AJ, 111, 1025
Murphy, T. W., Soifer, B. T., Matthews, K., & Armus, L. 2001, ApJ, 559, 201
Murray, N., Ménard, B., & Thompson, T. A. 2011, ApJ, 735, 66, 1005.4419
Naab, T., & Ostriker, J. P. 2006, MNRAS, 366
Rich, J. A., Kewley, L. J., & Dopita, M. A. 2014, ApJ, 781, L12, 1310.3441
Rich, J. A., Torrey, P., Kewley, L. J., Dopita, M. A., & Rupke, D. S. N. 2012, ApJ, 753, 5, 1204.5520
Rousselot, P., Lidman, C., Cuby, J.-G., Moreels, G., & Monnet, G. 2000, A&A, 354, 1134
Roškar, R. et al. 2015, MNRAS, 449, 494, 1406.4505
Rupke, D. S., Veilleux, S., & Sanders, D. B. 2005, ApJS, 160, 115
Rupke, D. S. N., & Veilleux, S. 2013, ApJ, 775, L15, 1308.4988
——. 2015, ApJ, 801, 126, 1411.3744
Rupke, D. S. N., Veilleux, S., & Baker, A. J. 2008, ApJ, 674, 172
Sanders, D. B. et al. 1986, ApJ, 305, L45
——. 1988a, ApJ, 325, 74
Sanders, D. B., Soifer, B. T., Elias, J. H., Neugebauer, G., & Matthews, K. 1988b, ApJ, 328, L35
Scoville, N. 2003, Journal of the Korean Astronomical Society, 36, 167
Soifer, B. T. et al. 1986, ApJ, 303, L41
Solomon, P. M., Downes, D., Radford, S. J. E., & Barrett, J. W. 1997, ApJ, 478, 144
Soto, K. T., & Martin, C. L. 2010, ApJ, 716, 332
——. 2012, ApJS, 203, 3
Soto, K. T., Martin, C. L., Prescott, M. K. M., & Armus, L. 2012, ApJ, 757, 86
Springel, V., Di Matteo, T., & Hernquist, L. 2005, MNRAS, 361, 776
Surace, J. A., Sanders, D. B., & Evans, A. S. 2000, ApJ, 529, 170, astro-ph/9909085
Thompson, T. A., Quataert, E., & Murray, N. 2005, ApJ, 630, 167
Thompson, T. A., Quataert, E., Zhang, D., & Weinberg, D. 2015, ArXiv e-prints, 1507.04362
Tremaine, S. et al. 2002, ApJ, 574, 740
Veilleux, S., Kim, D.-C., & Sanders, D. B. 2002, ApJS, 143, 315
Veilleux, S. et al. 2013, ApJ, 776, 27, 1308.3139
Veilleux, S. et al. 2009, ApJS, 182, 628
Wizinowich, P. et al. 2006, PASP, 118, 297
Zamojski, M. et al. 2011, ApJ, 730, 125, 1101.2368